Advanced Materials

ADVANCED MATERIALS
www.advmat.de

RESEARCH ARTICLE

In Situ Single-Atom Decoration of Transition Metal Dichalcogenides by Millisecond Flash Thermal Synthesis Toward High Performance Room Temperature Chemiresistors

Euichul Shin[1] | Jacob Choe[1] | Wonjun Choi[1] | Sanghyeon Park[1] | Chungseong Park[1] | Jong Won Baek[1] | Sungyoon Woo[1] | Mingyu Sagong[1] | Minsu Kim[1] | Chan-Woo Lee[2] | Ju Li[3,4] | Jong Min Yuk[1] | Sung-Yool Choi[5] | Dong-Ha Kim[6] | Il-Doo Kim[1]

[1]Department of Materials Science and Engineering, Korea Advanced Institute of Science and Technology, Daejeon, Republic of Korea | [2]Department of Energy and Materials Engineering, Dongguk University, Seoul, Republic of Korea | [3]Department of Nuclear Science and Engineering, Massachusetts Institute of Technology, Cambridge, Massachusetts, USA | [4]Department of Materials Science and Engineering, Massachusetts Institute of Technology, Cambridge, Massachusetts, USA | [5]School of Electrical Engineering, Korea Advanced Institute of Science and Technology, Daejeon, Republic of Korea | [6]Department of Materials Science & Chemical Engineering, Hanyang University-ERICA, Ansan, Gyeonggi-do, Republic of Korea

Correspondence: Dong-Ha Kim (dongha0507@hanyang.ac.kr) | Il-Doo Kim (idkim@kaist.ac.kr)

Received: 31 January 2026 | **Revised:** 10 September 2026 | **Accepted:** 16 September 2026

Keywords: flash thermal synthesis | gas sensors | photothermal effect | single atom catalysts | transition metal dichalcogenides

ABSTRACT

Transition metal dichalcogenides (TMD) are attractive for adsorption-driven reactions, yet their activity is strongly site-dependent. Activity is concentrated at edge motifs, whereas most exposed area resides on inert basal planes. Dual-site designs that enrich edges while activating basal planes with catalysts remain challenging to realize without coarsening and metal aggregation during thermal processing. Here, an intense pulsed light-driven flash thermal synthesis route is demonstrated that directly converts ammonium tetrathiomolybdate ($(NH_4)_2MoS_4$) into few-layer, edge-rich MoS_2 nanoflakes (FTS-MoS_2) within 10 ms pulse in ambient-air. Ultrafast photothermal shock (1192–1811°C; ~10^5/10^4°C s^{-1} heating/cooling rates) suppresses in-plane coarsening and out-of-plane stacking, while Pt, Ir, or Au single atoms are uniformly anchored on MoS_2 via rapid metal-sulfur coordination without aggregation. As a proof-of-concept, FTS-MoS_2 exhibits a 23.6-fold higher NO_2 response at 5 ppm than solvothermally synthesized MoS_2. Pt single atom functionalization (FTS-Pt_{SA}-MoS_2, 1.2 wt%) further boosts the response by 22.8-fold versus pristine FTS-MoS_2 and achieves 100.8% response toward 400 ppb NO_2 at room temperature. Density functional theory supports enhanced NO_2 adsorption and charge transfer on FTS-Pt_{SA}-MoS_2. With a low electrical energy input (8.6 kJ g^{-1}) and scalable irradiation, ultrafast FTS enables industrially relevant active-site and single-atom engineering in TMDs for high-performance gas sensors.

1 | Introduction

Transition metal dichalcogenides (TMDs) have emerged as versatile low-dimensional materials whose electronic structure and surface chemistry can be engineered for catalysis, sensing, and energy conversion [1]. Among them, molybdenum disulfide (MoS_2) is particularly attractive because its surface can host a wide range of adsorption and charge-transfer processes while maintaining chemical robustness [2, 3]. However, a key materials-level principle is that MoS_2 activity is strongly site-dependent.

Edge sites are generally far more reactive than basal planes, and thermodynamics often favors basal plane exposure during growth, limiting the density of accessible active sites [4, 5]. As a result, downsizing MoS_2 into edge-rich nanoflakes is a direct and powerful strategy to maximize active-site density per mass and to accelerate surface reaction kinetics.

Despite the clear design purpose, controlling MoS_2 at the nanoscale remains challenging. Many conventional synthesis routes (e.g., solvothermal growth, postsulfurization, and furnace-based conversions) require long reaction times and extended thermal budgets, which commonly promote coarsening and structural reorganization [6]. In situ microscopy studies have shown that MoS_2 can grow and enlarge through temperature-driven processes such as merging and ripening-like evolution, ultimately increasing lateral size and reducing the ratio of edge exposure [7]. Consequently, achieving nano-lateral size is still challenging, especially when the synthesis must be performed under prolonged annealing. Although edge enrichment enhances activity, integrating a basal-plane activation strategy further enhances catalytic activity, including in the presence of vacancies and additives. Functionalization via the incorporation of catalytic species, particularly single-atom catalysts (SACs), offers a powerful strategy to boost basal plane activity with maximum atomic efficiency. However, stabilizing and retaining isolated metal atoms on 2D supports is intrinsically difficult because metal species can migrate and aggregate, especially under thermal treatment [8]. Conventional synthesis routes for SACs on MoS_2 often involve prolonged high-temperature treatments under reducing conditions, which can induce lateral domain growth, multilayer formation, or agglomeration of metal atoms, ultimately challenging the synthesis for nanoscale integrity of the MoS_2 host [9]. Therefore, achieving in situ anchoring of SACs while maintaining the nanoscale morphology of MoS_2 is critical for the realization of highly active TMD-based functional materials.

Ultrafast thermal treatment techniques have emerged as promising strategies for nanoscale catalyst synthesis by enabling rapid nucleation while suppressing undesired growth [10]. Among ultrafast approaches, electromagnetic irradiation-based annealing (e.g., microwaves, lasers, and broadband light) is particularly attractive due to noncontact and integration of diverse substrates. However, each modality presents distinct trade-offs. Microwave processing can provide volumetric heating, yet the temperature profile is often sensitive to cavity field distributions [11]. Laser annealing delivers extremely high local intensities but typically relies on beam scanning and overlap strategies to achieve large-area processing [12]. By contrast, xenon-flash/intense pulsed light (IPL) annealing offers millisecond-duration broadband irradiation with high radiant energy density and scalable, large-area exposure, enabling strong photothermal heating under short processing durations [13]. Such flash-type thermal shock processing has enabled the synthesis of single-atom catalysts and high-entropy nanomaterials by confining high-temperature exposure to millisecond durations [14–17]. Although flash thermal synthesis (FTS) process has been exploited for carbon and oxide materials, its extension to TMDs has thus far primarily focused on ultrafast synthesis and phase/heterostructure engineering, whereas catalytic functionalization, particularly the integration of atomically dispersed catalytic sites, remains rarely explored [18, 19].

Here, we demonstrate single-step FTS strategy (1192°C–1811°C peak temperature, 10 ms irradiation, and 10^4–10^5°C s^{-1} ramping rates) that directly converts ammonium tetrathiomolybdate ($(NH_4)_2MoS_4$) into edge-rich MoS_2 nanoflakes, while simultaneously enabling the uniform dispersion of noble-metal single atoms (e.g., Pt, Ir, and Au) on the MoS_2 framework under ambient air. The ultrafast thermal kinetics facilitate the formation of MoS_2 with a high edge-to-volume ratio and promote rapid metal-sulfur coordination of isolated atoms. To demonstrate the practical feasibility of this approach, we investigated chemiresistive gas sensing performance of the FTS-based MoS_2 (FTS-MoS_2) and single atom functionalized MoS_2 (FTS-M_{SA}-MoS_2). Notably, FTS-MoS_2 shows a 23.6-fold higher NO_2 response than solvothermally synthesized MoS_2. Pt single atom functionalization (1.2 wt%) further enhances the response by 22.8-fold at room temperature at 400 ppb NO_2, achieving a limit of detection (LOD) of 17.2 ppb. The highly active sites for gas molecules on TMDs can be broadly expanded to various electrocatalysis fields by diversifying single atoms and extending to other TMD materials, as these properties significantly enhance gas adsorption and desorption characteristics crucial for catalytic performance. In addition, this rapid TMDs synthesis method could realize low-cost, mass production of nanocrystalline TMDs at only 8.6 kJ g^{-1} in electrical energy.

2 | Results and Discussion

2.1 | Flash Thermal Synthesis of TMDs

Figure 1a schematically illustrates IPL-driven FTS of TMDs. First, 100 mg of ammonium tetrathiomolybdate (ATTM, $(NH_4)_2MoS_4$) was uniformly dispersed in 1 mL of deionized water through ultrasonication. Then, 100 µL of the ATTM solution was drop-cast onto a microscope glass slide and dried on a hot plate at 80 °C (Figure S1). The xenon lamp used in the intense pulsed light (IPL) process emits light over a broad wavelength range of approximately 300–1000 nm (Figure S2). Within this range, ATTM exhibits strong visible light absorption from 400 to 800 nm, as confirmed by the absorption spectra in Figure S3. The absorbed energy was estimated using photon counts (Figure S2) and absorbance (Figure S3). Notably, visible light accounted for 78.7% of the total irradiation during the IPL process, as indicated in Figure S4. This high optical absorbance enables efficient photothermal heating via nonradiative relaxation [20, 21]. After the IPL process, the samples were purified by centrifugation at 8000 rpm for 10 min with deionized water and ethanol. According to previous reports, ATTM thermolysis proceeds via a MoS_3 intermediate with the release of NH_3 and H_2S, followed by conversion to MoS_2 at higher temperatures [22]. At sufficiently high temperatures, sulfur loss/sublimation can generate S vacancies in MoS_2 [23]. After IPL irradiation, visible redistribution of the reacted material was observed on the substrate (Figure S5). Together with the decreasing recovered solid mass before washing at higher FTS powers (Note S1), this observation suggests that additional process-associated loss occurs during the FTS pulse, potentially through volatilization and physical material ejection. Figure 1b shows temperature-time profiles under a single 10 ms IPL pulse at lamp power settings of 1000, 1500, and 2000 W. The resulting peak temperatures reached approximately 1192°C, 1481°C, and 1811°C, respectively, depending on the irradiation

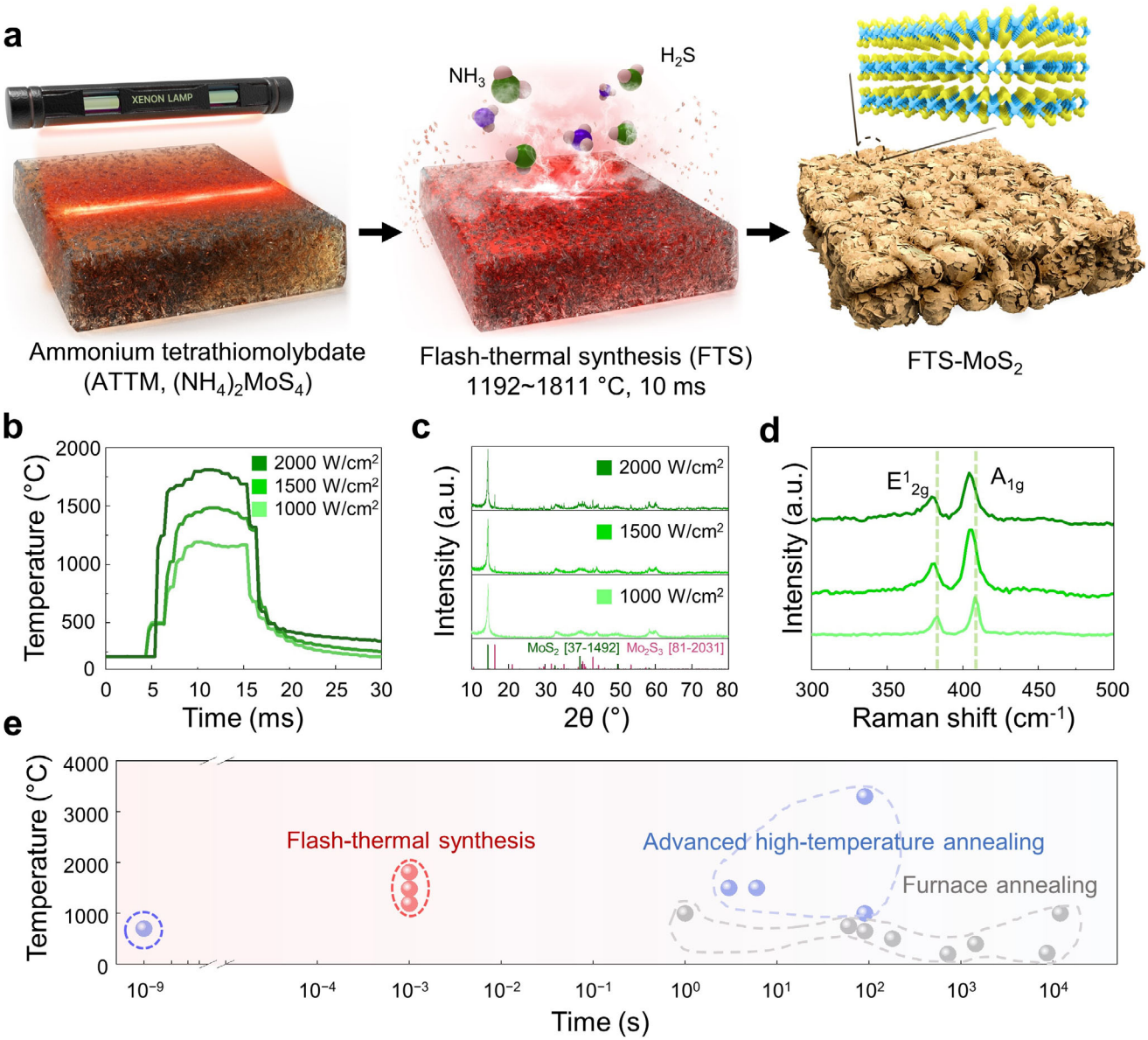

FIGURE 1 | (a) Schematic illustration of the synthesis of MoS_2 via flash thermal synthesis (FTS). (b) Photothermal temperature-time profiles, (c) XRD patterns, and (d) Raman spectra of FTS-MoS_2 synthesized under power densities of 1000, 1500, and 2000 W cm^{-2}. (e) Comparison of the synthesis time and temperature between FTS, advanced high-temperature annealing, and conventional furnace annealing. The detailed temperature and time parameters are summarized in Table S1.

energy. FTS-based ultrafast heating/cooling of the ATTM coating (~10^5°C s^{-1} heating rate; ~10^4°C s^{-1} cooling rate; Figure S6) kinetically suppresses excessive growth, enabling few-layer MoS_2 nanoflakes (FTS-MoS_2). Scanning electron microscopy (SEM) images show spherical secondary particles assembled from small MoS_2 nanoflakes (Figures S7 and S8). These structures are attributed to the ultrafast reaction kinetics of the FTS process, which suppresses the lateral growth of MoS_2. In addition, transmission electron microscopy (TEM) was employed to investigate the structural characteristics of FTS-MoS_2, particularly its high edge-to-volume ratio, predominantly short clusters characterized by discontinuous, bent, disjointed, and curved basal planes, indicative of a highly defective structure (Figure S9). In contrast to the solvothermally synthesized MoS_2 (Figure S10), this morphology is consistent with millisecond-scale thermal shock kinetics, where the extremely short high-temperature annealing time limits diffusion-driven coarsening and interrupts lateral grain growth/coalescence, resulting in fragmented nanocrystalline domains [20]. These short and fragmented flakes suggest a high density of catalytically active edge sites. The high photothermal temperatures achieved under IPL irradiation were sufficient to decompose ATTM, resulting in the formation of crystalline MoS_2, as evidenced by distinct XRD patterns matching the standard PDF#37-1492 (Figure 1c). The crystallinity improved progressively with increasing irradiation energy, which can be attributed to the corresponding increase in FTS temperature (Figure S11). In addition, as the photothermal temperature increased, sulfur-deficient conditions generated during ATTM decomposition promoted the formation of a Mo_2S_3 phase (PDF#81-2031), which the ultrafast cooling process could kinetically retain [24]. Notably, although

the XRD patterns indicate the presence of this characteristic Mo_2S_3 phase, the XPS spectra are dominated by Mo^{4+} (Mo $3d_{5/2}$ at ~229.2–229.5 eV) and S^{2-} (S 2p at ~162.0–162.3 eV), together with a minor MoO_x contribution arising from surface oxidation (Figure S12) [25]. The absence of crystalline MoO_x peaks in XRD suggests that this oxidized component is surface-limited and/or amorphous rather than a bulk oxide phase. This surface-limited oxidation is due to the millisecond-scale thermal profile, in which the 10 ms of processing followed by rapid quenching restricts oxygen diffusion and suppresses extensive bulk oxidation (Figure S13) [26]. The surface of the resulting materials is predominantly composed of MoS_2 species with mild oxidation, whereas the Mo_2S_3 phase is more located in the inner sites in the materials and therefore is detected by XRD rather than by XPS. In this regard, the ultrafast FTS process generates a temperature gradient across the precursor domain, such that the hotter interior region favors the formation of the sulfur-deficient Mo_2S_3 phase, while the outer region is converted to MoS_2 and partially oxidized upon exposure to ambient air. Such spatially heterogeneous phase evolution is also consistent with previous flash-heating studies on ATTM/carbon systems, where an interior of high-temperature-derived α-MoC and an exterior of relatively low-temperature-derived MoS_2 were formed under FTS, giving rise to a core-shell heterostructure [27]. Raman spectroscopy further confirmed the formation of 2H-MoS_2 (Figure 1d). Two characteristic peaks at 383 and 408 cm^{-1} were observed, corresponding to the in-plane (E^1_{2g}) and out-of-plane (A_{1g}) vibrational modes of 2H-MoS_2, respectively. As the irradiation energy increased, the E^1_{2g} peak shifted to 381 cm^{-1} and the A_{1g} peak to 404 cm^{-1}, indicating a redshift in both vibrational modes due to lattice thermal expansion and anharmonic effects owing to sulfur vacancy formations. In addition, the weak but discernible peaks at 227 and 454 cm^{-1}, corresponding to the LA(M) and 2LA(M) modes, respectively, further indicate the defect-rich nature of FTS-MoS_2 (Figure S14). These sulfur vacancies became more pronounced at higher photothermal temperatures under intense irradiation [28]. X-ray photoelectron spectroscopy (XPS) analysis further suggested progressive sulfur deficiency with increasing irradiation energy, as reflected by a decrease in the S:Mo ratio from 1.996 (1000 W) to 1.990 (1500 W) and 1.920 (2000 W) (Figure S15) [29]. In addition, atomic resolution STEM line profiles reveal a systematic contraction of the nearest-neighbor Mo–Mo spacing (mean of 40–50 measured distances), decreasing from 3.22 to 3.12 and 2.96 Å as the irradiation energy increased (Figure S16). This trend is consistent with local lattice relaxation/strain accumulation around sulfur vacancies, where adjacent Mo atoms relax inward upon S removal [30, 31]. DFT calculations show that introducing sulfur vacancies leads to a reduced Mo–Mo distance, reproducing the experimentally observed contraction and supporting vacancy-induced lattice strain as the origin of the measured Mo–Mo spacing change (Figure S17).

Altogether, this FTS route offers access to high temperatures and faster ramping rates than many reported TMD synthesis/annealing approaches (Figure 1e and Table S1). Conventional furnace heating typically operates at temperatures around 1000°C and requires several hours to synthesize TMDs where large amounts of energy are used to maintain the temperature of the chamber. Although laser annealing has been reported to reach temperatures of ~700°C within 2 ns, the processed area (spot size) is limited to 20 μm [32]. In comparison, the FTS method rapidly achieves temperatures up to 1811°C within just 10 ms while providing a significantly larger irradiation area of up to 75 cm^2, determined by the size of the xenon lamp (5 × 15 cm in this system). Owing to ultrafast ramping, direct precursor-to-product conversion, and millisecond/large processing, the FTS-based synthetic method is energy-efficient (8.6–15.5 kJ g^{-1}) and enables MoS_2 synthesis in ambient air (Notes S1 and S2).

2.2 | Flash Thermal Synthesis of SAC-TMDs

Among the irradiation conditions, we selected the 2000 W setting as an optimized FTS condition because it provides a sufficiently high temperature (> 1700°C) to drive the synthesis of defective MoS_2 nanoflakes and simultaneously decomposition of noble metal precursors within a single 10 ms pulse (Figure 2a). Importantly, the millisecond-duration annealing and rapid quenching can kinetically suppress metal aggregation, enabling atomically dispersed metal species to form on the basal planes of MoS_2. Given that isolated metal atoms can be stabilized in different coordination environments on the MoS_2 surface, we selected representative noble metals to demonstrate the versatility of the FTS-based SAC functionalization strategy [33, 34]. Noble metal precursors, such as $H_2PtCl_6{\cdot}6H_2O$, $IrCl_3$, and $HAuCl_4{\cdot}3H_2O$ were introduced into the ATTM solution to achieve one-step SAC functionalization during FTS. To remove residual precursor species, the samples were thoroughly washed with ethanol prior to characterization (Figure S18). To investigate the energetically favorable adsorption site of the Pt, Ir, and Au single atom on the basal plane, density functional theory (DFT) calculations were conducted. To model the basal plane of FTS-MoS_2, the slab model with (001) plane was constructed from the bulk 2H-MoS_2 structure, including Mo_2S_3 and sulfur vacancies (Figure S19). Unique adsorption sites were defined on the surface of the FTS-MoS_2 slab model (Figure 2b), consisting of Mo_{near}, Mo_{mid}, and Mo_{far} site where the single atom is located on the top of Mo atoms near, at midrange, and far from the sulfur vacancy, respectively, and a S site where the single atom is located on a top of S atom. Figure 2c shows the adsorption energies of Pt, Ir, and Au on the defined adsorption sites. The energetically most stable structures for every single atom are shown in Figure 2d. For Pt and Ir single atom, the Mo_{mid} site is preferred adsorption site with a large difference of adsorption energy (0.68 and 1.51 eV for Pt and Ir, respectively). However, the Au single atom prefers the S site with a relatively small energy difference (0.24 eV), indicating a relatively high probability of occupying other adsorption sites as well (Figure S20). Figure 2e–g provide microscopic and spectroscopic evidence for atomically dispersed Pt on MoS_2 (FTS-Pt_{SA}-MoS_2, Figure S21). In the Pt 4f region, the Pt $4f_{7/2}$ component at 73.09 eV is shifted to higher binding energy relative to metallic Pt (71 eV), consistent with cationic Pt species ($Pt^{\delta+}$) interacting with sulfur in the MoS_2 (Figure S22) [35]. Bright contrast spots in the high-angle annular dark-field scanning transmission electron microscopy (HAADF-STEM) images were attributed to Pt single atoms, which were further verified by line scan profiling (Figure 2f) and 3D contour mapping (Figure 2g). Similarly, the formation of Ir (Figure 2h–j and Figure S23) and Au (Figure 2k–m and Figure S24) single atoms on MoS_2 was confirmed. In the XPS analysis, the peaks of Ir and Au were located at 62.22 and 86.02 eV for FTS-Ir_{SA}-MoS_2 and FTS-Au_{SA}-MoS_2, respectively, corresponding to $Ir^{\delta+}$ and $Au^{\delta+}$ states. These peaks

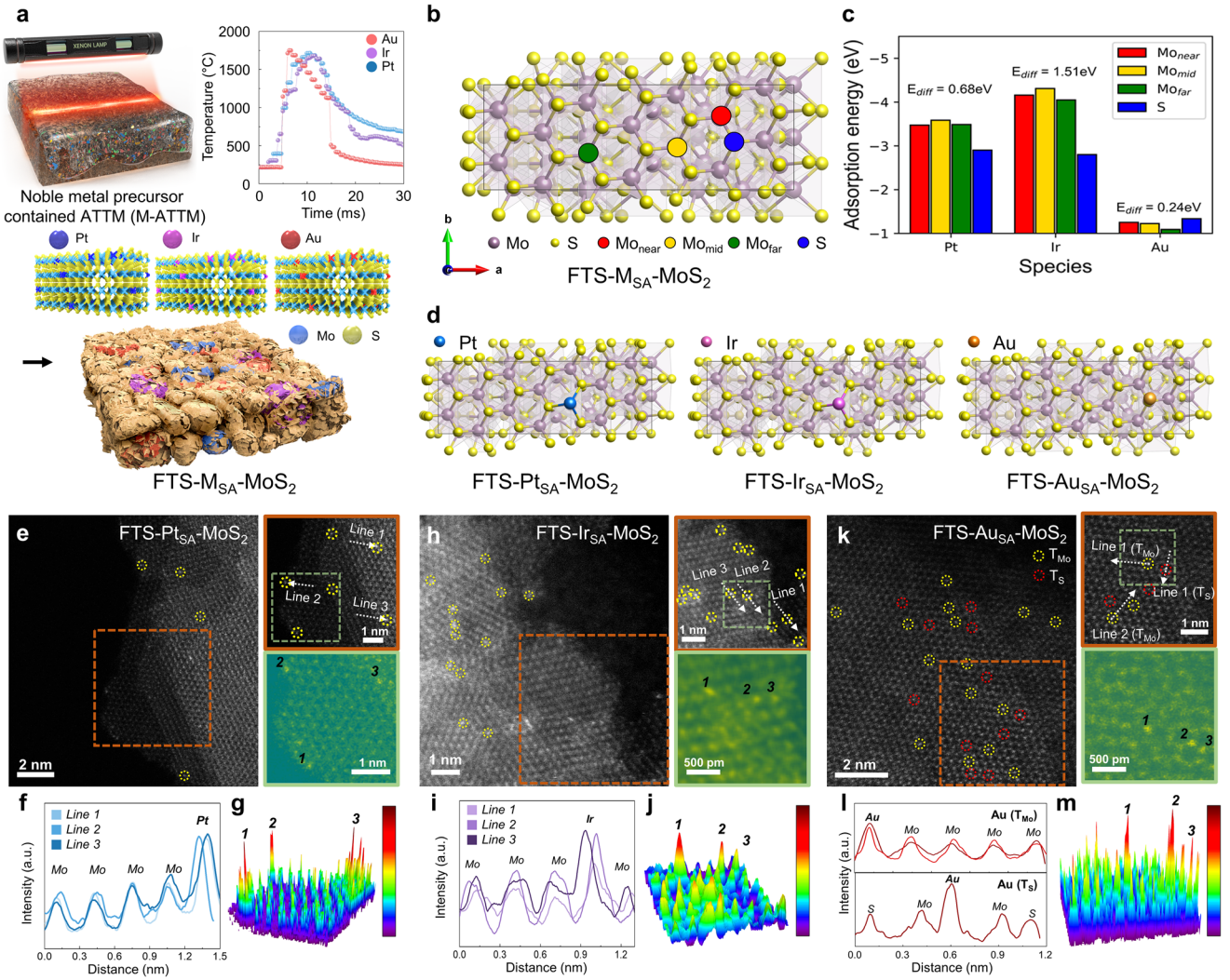

FIGURE 2 | (a) Schematic illustration of metal-containing ATTM (M-ATTM) to produce single atom functionalized MoS_2 via FTS (FTS-M_{SA}-MoS_2; M = Pt, Ir, and Au) and photothermal temperature-time curves. (b) FTS-MoS_2 slab model and adsorption sites considered in DFT calculations (c) Calculated adsorption energies of Pt, Ir, and Au at top of Mo_{near}, Mo_{mid}, Mo_{far}, and S sites. (d) DFT-optimized configurations of Pt, Ir, and Au single atoms on MoS_2 at their preferred adsorption sites. HAADF-STEM images and their corresponding line profile, and 3D-contour mapping images for (e-g) FTS-Pt$_{SA}$-MoS_2, (h–j) FTS-Ir$_{SA}$-MoS_2, and (k–m) FTS-Au$_{SA}$-MoS_2.

suggest the formation of strong metal-chalcogen interactions (Figures S25 and S26) [36, 37]. The formation of isolated atoms without detectable metallic properties is attributed to the ultrafast, nonequilibrium characteristics of the FTS process, which enables rapid precursor conversion/anchoring while kinetically suppressing coarsening that typically drives nanoparticle (NP) formation. High-power FTS (2000 W) led to sulfur deficiency at the MoS_2 surface (4%–8% by XPS, Figures S15 and S27). Notably, high-temperature desulfurization of MoS_2 is known to induce sulfur-deficient reconstructions [38]. Moreover, prior studies indicate that introducing isolated metal atoms can promote defect generation and structural/phase evolution in MoS_2, which may facilitate sulfur loss under ultrafast thermal shocks [39]. The excessive sulfur vacancies can lead to a phase change from MoS_2 to Mo_2S_3, especially in metastable conditions in ultrafast synthesis, as confirmed by XRD analysis (Figure S28), similar to the previous reports [27]. The Pt-, Ir-, and Au-functionalized FTS-MoS_2 exhibited no detectable metallic peaks, confirming that the noble metal species were atomically dispersed without the formation of metallic NPs (FTS-M_{SA}-MoS_2, M denotes Pt, Ir, and Au).

To identify the Pt loading regime that yields atomically dispersed species on FTS-MoS_2, we synthesized a series of FTS-Pt-MoS_2 with different nominal Pt contents. ICP-MS confirmed Pt loadings of 0.03, 0.5, 0.7, 1.2, and 3 wt%. The XRD analysis indicated the MoS_2 and Mo_2S_3 with all FTS-Pt-MoS_2 and exhibited no detectable metallic Pt peaks, which is consistent with the absence of Pt NPs and/or the detection limit of ultrasmall/low-loading Pt by XRD. (Figure 3a). Notably, the relative Mo_2S_3 contribution increased with increasing Pt loading, suggesting that Pt could facilitate sulfur depletion during the high-temperature FTS process and thereby promote the formation of sulfur-deficient Mo_2S_3. In addition, the electron spin resonance spectrum showed a strong signal at a g value of 2.21, indicating the presence of defect-related paramagnetic centers that may be associated with a sulfur-deficient local Mo-S environment, including sulfur-vacancy sites (Figure S29) [40]. Raman spectra further reveal

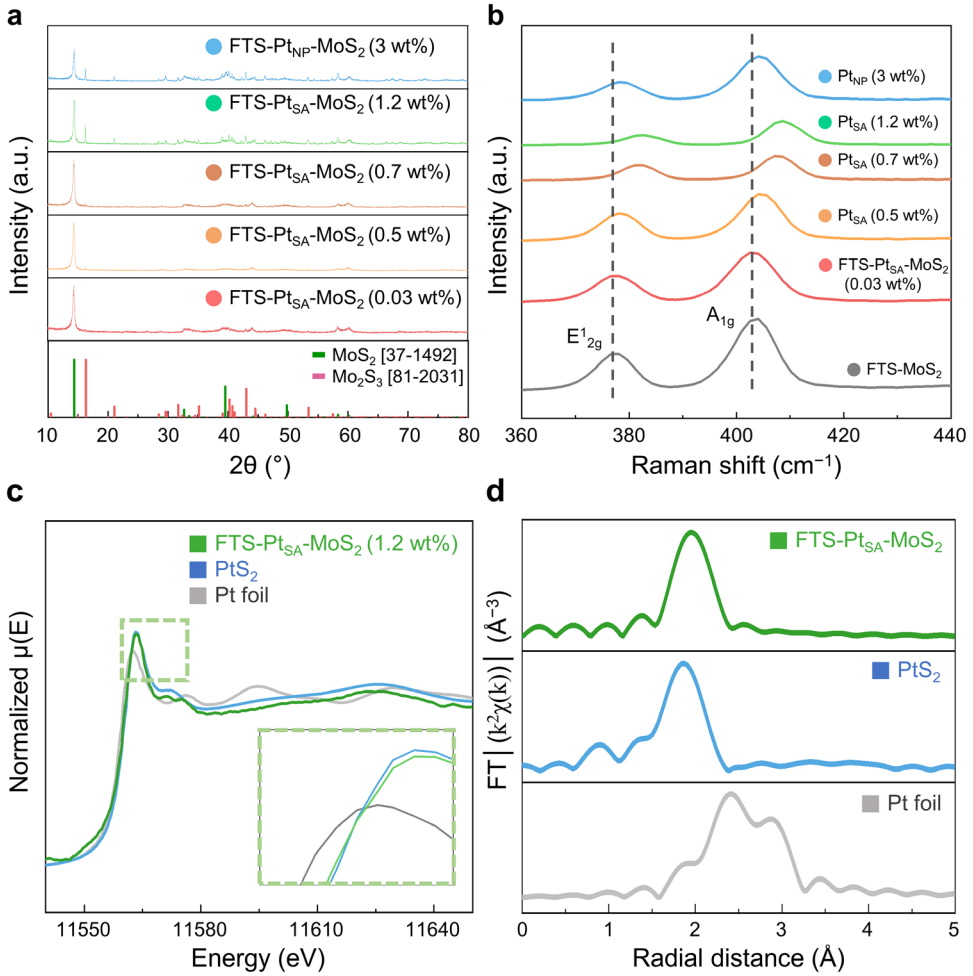

FIGURE 3 | (a) XRD patterns of FTS-Pt-MoS_2 synthesized with different Pt loadings (0.03, 0.5, 0.7, 1.2, and 3 wt%). (b) Raman spectra of FTS-MoS_2 and FTS-Pt-MoS_2. (c) Pt L_3-edge XANES spectra of FTS-Pt_{SA}-MoS_2 (1.2 wt%) compared with PtS_2 and Pt foil. (d) Fourier-transformed k^2-weighted EXAFS magnitude of FTS-Pt_{SA}-MoS_2 (1.2 wt%) with PtS_2 and Pt foil.

a Pt loading dependent shift of the E^1_{2g} and A_{1g} modes. The low loading (0.03 wt%) induces negligible changes, whereas intermediate loadings in the single atoms show blue shifts, consistent with charge-transfer/strain effects that are known to modulate MoS_2 phonon frequencies (Figure 3b) [41, 42]. At the highest Pt loading investigated (3 wt%), the Raman-shift trend was reversed, coinciding with the emergence of a metallic Pt component in XPS and Pt-containing nanoparticles in electron microscopy (Figures S30 and S31). These observations indicate a loading-dependent loss of atomic dispersion under the present FTS conditions. The formation of aggregated Pt species at 3 wt% may reflect an increased probability of Pt–Pt association relative to isolated stabilization as the surface Pt population increases. However, because the density and distribution of the available anchoring sites on FTS-MoS_2 were not independently quantified, a specific anchoring-capacity threshold cannot be assigned from the present data. Accordingly, the 1.2 wt% sample, which retained predominantly atomically dispersed Pt under the present FTS conditions, was selected as the representative sample for detailed structural characterization. X-ray absorption near-edge spectroscopy (XANES) and extended x-ray absorption fine structure (EXAFS) profiles were used to investigate the electronic structure and coordination of the Pt in FTS-Pt_{SA}-MoS_2 (1.2 wt%). The XANES analysis on FTS-Pt_{SA}-MoS_2 (1.2 wt%) shows that their Pt L_3 edge absorption energy values and White line intensities are significantly higher than that of metallic Pt foil, which indicating the Pt species in the FTS-Pt_{SA}-MoS_2 are dominantly in the oxidized state (Figures 3c and S32). These XANES results are consistent with the XPS analysis, further confirming that the Pt species in FTS-Pt_{SA}-MoS_2 are predominantly oxidized rather than metallic (Figure S33). The Fourier-transformed EXAFS of FTS-Pt_{SA}-MoS_2 exhibits a dominant peak at 1.9 Å, which can be attributed to the Pt-S scattering (Figure 3d). In addition, the corresponding EXAFS fitting results in both k-space and R-space, together with the Wavelet-transformed EXAFS contour analysis, further support a sulfur-coordinated local environment around Pt (Figure S34). The fitting results demonstrate that the Pt—S bond has an average bond length of 2.36 Å and an average coordination number of 3.2 in the FTS-Pt_{SA}-MoS_2 (Table S2). The first-shell Pt—S feature of FTS-Pt_{SA}-MoS_2 appears at a slightly higher R value than that of PtS_2, which may be attributed to the undercoordinated and locally distorted Pt—S environment of atomically dispersed Pt species [43].

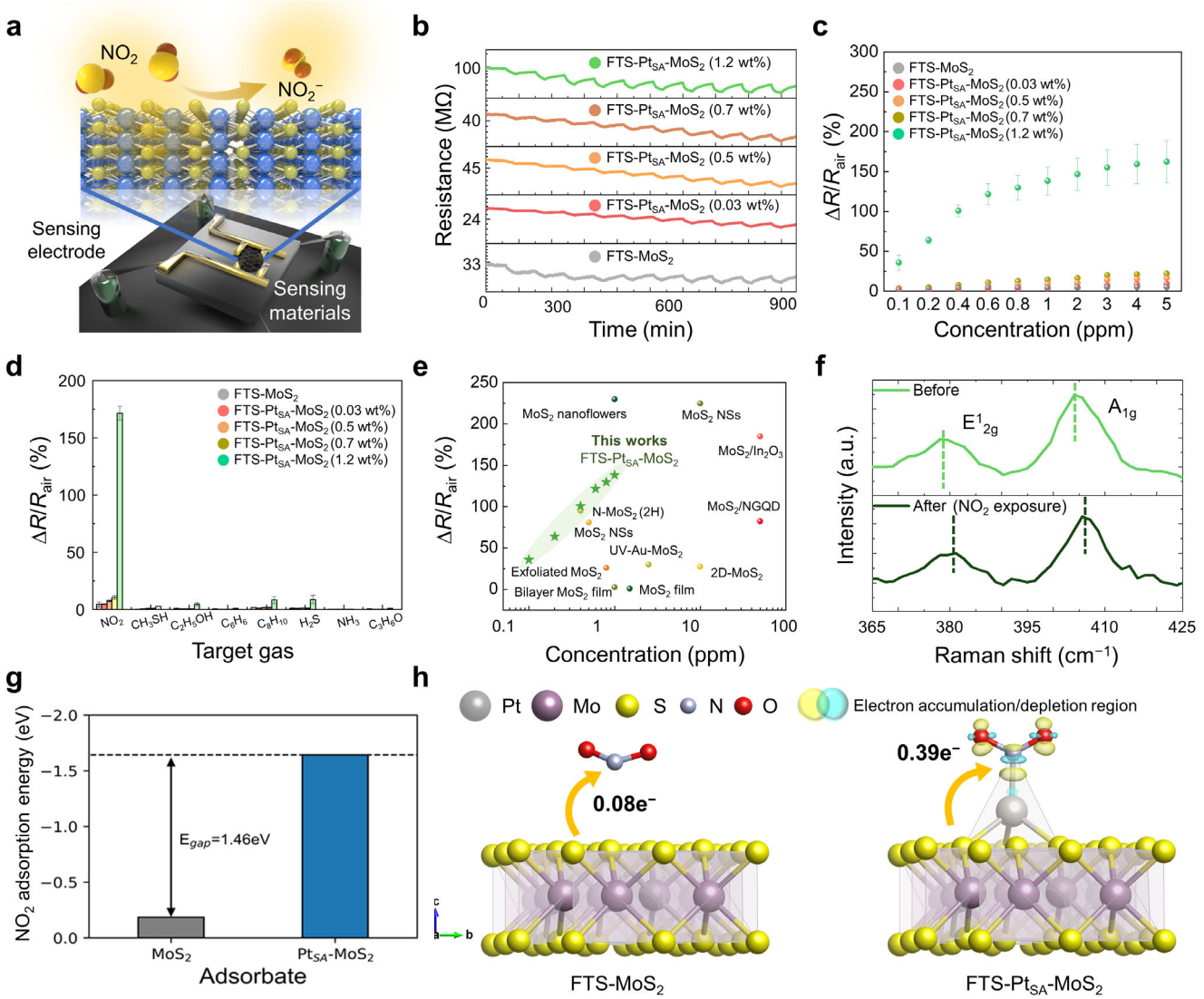

FIGURE 4 | (a) Schematic illustration of the Al_2O_3-based Au interdigitated-electrode device and the proposed charge-transfer sensing mechanism of NO_2 on FTS-MoS_2. (b) Dynamic resistance traces for FTS-MoS_2 and FTS-Pt_{SA}-MoS_2 under NO_2 exposure (0.1–5 ppm) at room temperature. (c) Dynamic gas sensing performance of FTS-MoS_2 and FTS-Pt_{SA}-MoS_2. (d) Selective sensing performances of FTS-MoS_2 and FTS-Pt_{SA}-MoS_2 toward 5 ppm gases. (e) Comparison of the NO_2 response values to the state-of-the-art MoS_2-based sensing materials. (f) Ex situ Raman spectra for FTS-Pt_{SA}-MoS_2 (1.2 wt%) before and after NO_2 exposure. (g) DFT-calculated adsorption energies of NO_2 on bare MoS_2 and Pt_{SA}-MoS_2. (h) Charge density difference for NO_2 adsorption on bare MoS_2 and Pt_{SA}-MoS_2, illustrating enhanced charge transfer mediated by Pt single atoms.

2.3 | Applications: Chemiresistive NO_2 Gas Sensors

To demonstrate the practical utility of FTS-derived MoS_2, chemiresistive NO_2 sensing performance was evaluated. From an environmental and occupational-health perspective, sensitive detection of NO_2 at low-ppm levels is important; notably, the United States Occupational Safety and Health Administration (OSHA) lists a ceiling permissible exposure limit of 5 ppm for NO_2. Accordingly, the development of highly sensitive sensing materials is crucial for accurate detection and regulatory compliance in environmental and occupational settings. Homemade gas sensors were fabricated by drop-coating of sensing material solutions onto custom Al_2O_3 substrates. The alumina substrates were patterned with interdigitated Au electrodes, featuring a width of 25 μm and a distance of 70 μm (Figure 4a). Since gas adsorption on MoS_2 is strongly site-dependent, edge-/defect-rich MoS_2 architectures typically exhibit higher reactivity than basal plane-dominant counterparts [4]. In addition, the sulfur vacancies serve as active sites for gas adsorption, further improving sensing performance [44]. Consistent with this concept, FTS-MoS_2, which has smaller lateral features and higher edge density than solvothermally synthesized MoS_2, exhibited a 23.6-fold higher response to 5 ppm NO_2, indicating that edge-rich nanoflakes effectively improve gas-surface interactions (Figures S9 and S35). In addition, the heterointerfaces, such as Mo_2S_3 and MoO_x, in the FTS-MoS_2 also contribute to the enhanced response toward oxidizing NO_2 through interfacial charge transfer and hole accumulation [45]. Furthermore, catalyst functionalization significantly contributed to the enhancement of sensing performance, underscoring its pivotal role in boosting both sensitivity and selectivity [46]. The gas sensing characteristics of

Pt-functionalized FTS-MoS_2 (FTS-Pt-MoS_2) were systematically compared to those of FTS-MoS_2, further highlighting the catalytic role of Pt in enhancing sensor performance (Figure 4b). FTS-MoS_2 exhibited a p-type-like sensing response, as indicated by a decrease in resistance upon NO_2 exposure and positive apparent Hall slopes obtained from fixed-contact Hall-effect measurements (Figures S36, S37, and Table S3). We note that this macroscopic response should not be assigned to a single microscopic origin. FTS-MoS_2 contains sulfur deficiency, surface-limited MoO_x species, MoS_2/Mo_2S_3 phase heterogeneity, and multiple interfacial environments, all of which can perturb carrier density and charge transport and may collectively contribute to the observed p-type-like behavior. FTS-MoS_2 and FTS-Pt_{SA}-MoS_2 sensors, with varying Pt loadings (0.03, 0.5, 0.7, and 1.2 wt%), were exposed to NO_2 at different concentrations from 0.1 to 5 ppm under dry conditions (Figure 4c). The responses 5.38%, 9.28%, 16.35%, 22.07%, and 162.44% were achieved from FTS-MoS_2 and FTS-Pt_{SA}-MoS_2 (0.03, 0.5, 0.7, and 1.2 wt%) to 5 ppm NO_2, respectively. Among them, FTS-Pt_{SA}-MoS_2 (1.2 wt%) exhibited the highest sensing performance due to its maximized catalytic effect of single Pt atoms. Notably, outstanding sensing performance was maintained down to low ppb-level concentrations, with a 100.8% response measured at 400 ppb NO_2, 22.8-fold higher response than FTS-MoS_2. At a higher Pt loading of 3 wt%, the excessive catalyst could hinder interactions with target gas molecules, resulting in a reduced sensing response (Figure S38). The FTS-MoS_2 exhibited excellent selectivity toward 5 ppm NO_2 when compared to other analytes at the same concentration, including CH_3COCH_3, NH_3, C_7H_8, C_8H_{10}, C_6H_6, and C_2H_5OH (Figures 4d and S39). To support the selectivity results shown in Figure 4d, additional DFT calculations of the adsorption energies and Bader charge differences were conducted for seven gas molecules (CH_3SH, C_2H_5OH, C_6H_6, C_8H_{10}, H_2S, NH_3, and C_3H_6O) to compare these results with those of NO_2. Two adsorption configurations were considered for each molecule (Figure S40). As shown in Figure S41, for the most stable adsorption structures, the adsorption energies of each molecule were calculated for CH_3SH (−1.69 eV), C_2H_5OH (−0.92 eV), C_6H_6 (−1.46 eV), C_8H_{10} (−1.54 eV), H_2S (−1.40 eV), NH_3 (−1.32 eV), and C_3H_6O (−0.99 eV). These values are comparable to those of NO_2 (−1.64 eV) or, in some cases, stronger by up to 0.63 eV. Figure S42 shows the Bader charge differences of the gas molecules on FTS-Pt_{SA}-MoS_2. Among the eight adsorbates, CH_3SH (−0.25 e^-), C_2H_5OH (−0.11 e^-), C_6H_6 (−0.04 e^-), C_8H_{10} (−0.08 e^-), H_2S (−0.18 e^-), NH_3 (−0.18 e^-), and C_3H_6O (−0.07) exhibit negative charge differences, indicating that these gas molecules are oxidized upon adsorption. In contrast, NO_2 shows a positive charge difference of 0.39 e^-, indicating electron transfer from FTS-Pt_{SA}-MoS_2 to the adsorbed NO_2 molecule. These calculations indicate that NO_2 exhibits a distinct electron-withdrawing interaction among the examined adsorbates on the FTS-Pt_{SA}-MoS_2 model. This preferential charge-transfer behavior is consistent with the enhanced NO_2 response and selectivity, although it does not by itself establish the microscopic origin of the macroscopic p-type-like transport response. Furthermore, the sensing performance of FTS-MoS_2 was evaluated under varying relative humidity (RH) levels and detection limits, along with an evaluation of long-term operational stability. Although excessive H_2O adsorption can hinder NO_2 sensing by competing for active sites, adsorbed water can also modify the surface charge state of MoS_2 and increase the baseline resistance by acting as an electron-trapping species [47]. The baseline resistance increased under 50% RH and 75% RH for all samples, while the recovery characteristics of FTS-MoS_2 and FTS-Pt_{SA}-MoS_2 (0.03, 0.5, 0.7, and 1.2 wt%) were clearly improved (Figure S43). Water-assisted surface charge transfer and the partial suppression of direct NO_2 chemisorption can improve the recovery behavior at room temperature. In particular, the response of FTS-Pt_{SA}-MoS_2 (1.2 wt%) increased from 158.23 in dry air to 193.37 at 50% RH and 182.68 at 75% RH, indicating a humidity-assisted enhancement of room-temperature NO_2 sensing under moderate RH conditions (Figure S44). Although the dual-site activation strategy effectively enhances NO_2 adsorption and sensing response, the recovery behavior remains limited at room temperature owing to the intrinsic adsorption–desorption trade-off. These results suggest that additional activation strategies, such as light irradiation, mild thermal input, water-assisted modulation, or further tuning of the intrinsic surface activity, are required to improve reversibility. Notably, the FTS-Pt_{SA}-MoS_2 (1.2 wt%) sensors exhibited a low limit of detection (LOD) of 17.2 ppb (Figure S45). Furthermore, it consistently maintained stable sensitivity even after repeated exposure and recovery cycles (25 cycles) toward 5 ppm NO_2, as shown in Figure S46. In addition, FTS-Pt_{SA}-MoS_2 (1.2 wt%) maintained a robust sensing response under ambient air, exhibiting only 2.6% degradation after 3 weeks (Figure S47). To elucidate the stable sensing performance, post-sensing XRD, XPS, and HAADF-STEM analyses were conducted, confirming the preservation of the MoS_2 phase and atomically dispersed Pt species after 25 sensing cycles, despite a mild increase in surface oxidation (Figures S48-S51). This performance indicated superior sensitivity and durability, making it suitable for practical applications requiring long-term operation and high detection accuracy. Overall, FTS-Pt-MoS_2 demonstrated selective NO_2 detection with improved sensing performance, showing superior performance compared with other MoS_2-based and SAC-based room temperature operating NO_2 sensors reported in the literature (Figure 4e and Tables S4, S5).

To elucidate the sensing mechanism of NO_2 on the FTS-Pt-MoS_2 surface, ex situ Raman spectroscopy was conducted after NO_2 exposure. FTS-MoS_2 exhibited a decrease in resistance upon NO_2 exposure, consistent with the p-type-like chemiresistive response observed under the present measurement conditions (Figure 4b). Because the FTS-derived material contains sulfur deficiency, surface oxidation, MoS_2/Mo_2S_3 phase heterogeneity, and multiple interfaces, the macroscopic resistance response likely reflects the combined contribution of these structural and electronic features rather than a single carrier-generation mechanism. NO_2 acts as an electron-accepting adsorbate, and its interaction with the sensing surface can be represented in a simplified form as:

$$NO_2\,(ads) + e^- \rightarrow NO_2^-\,(ads) \quad (1)$$

For FTS-Pt-MoS_2, strongly adsorbed NO_2 acts as an oxidant, extracting electrons from MoS_2 and enhancing charge transfer.

After NO_2 exposure, the Raman modes shifted to higher wavenumbers relative to those before exposure (Figure 4f and Figure S52). This ex situ blueshift indicates an overall exposure-induced perturbation of the MoS_2 vibrational/electronic state and is consistent with electron depletion; however, contributions from strain, defects, and structural heterogeneity cannot be excluded. Importantly, ex situ Raman spectroscopy does not

provide site-specific information and therefore cannot directly identify Pt single atoms as the NO_2 adsorption sites. The specific role of Pt single atoms was instead evaluated using DFT calculations for NO_2 adsorption on bare FTS-MoS_2 and FTS-Pt_{SA}-MoS_2 slab models. To consider the various NO_2 adsorption configurations in each surface model, adsorption energies were evaluated for 3 and 2 adsorption configurations on bare FTS-MoS_2 (Figures S53 and S54) and FTS-Pt_{SA}-MoS_2 (Figures S55 and S56) slab models, respectively. Figure 4g shows the representative adsorption energies of NO_2 for each model, demonstrating the stronger adsorption energy of NO_2 on FTS-Pt_{SA}-MoS_2, with a significant energy difference (1.46 eV) relative to the bare FTS-MoS_2. This calculation supports a preferential NO_2 interaction in the presence of the Pt single atom. To investigate the mechanism of enhanced NO_2 adsorption on Pt single atoms, Bader charge analysis and charge density difference maps were employed (Figure 4h) [48]. In the bare FTS-MoS_2 model, NO_2 adsorption resulted in a charge transfer of 0.08 e^- from MoS_2 to NO_2. In contrast, the FTS-Pt_{SA}-MoS_2 model showed a charge transfer of 0.39 e^- from the Pt_{SA}-MoS_2 to NO_2. Additionally, charge density difference maps demonstrate that charge transfer between the Pt single atom and NO_2 is significantly larger than that between the MoS_2 and NO_2. Together, these DFT results provide computational support for enhanced NO_2 adsorption and charge transfer associated with Pt single-atom functionalization. The FTS-Ir_{SA}-MoS_2 and FTS-Au_{SA}-MoS_2 showed similar enhancements in NO_2 adsorption and charge redistribution, supporting the enhanced NO_2 selectivity and sensing responses (Figures S57–S59). These results suggest that the FTS strategy is broadly applicable to diverse single-atom functionalization on MoS_2 and that catalytic tuning of the single-atom species can be used to tailor gas adsorption/desorption and sensing behavior.

3 | Conclusion

In summary, we demonstrate that IPL-driven FTS based on millisecond-scale photothermal shock provides a simple, energy-efficient, and scalable route to engineer highly active sites in MoS_2 under ambient air conditions. This process simultaneously suppresses lateral grain growth and yields edge-abundant and sulfur vacancy-rich few-layer MoS_2 nanoflakes. Moreover, when noble-metal precursors are introduced, the same one-step FTS enables in situ anchoring of atomically dispersed Pt, Ir, and Au single atoms without detectable nanoparticle formation up to an optimal loading (e.g., 1.2 wt% Pt). As a proof-of-concept application, FTS-MoS_2 exhibits a 23.6-fold higher NO_2 response than solvothermally synthesized MoS_2, while Pt single atom functionalization (FTS-Pt_{SA}-MoS_2, 1.2 wt%) further boosts the response 22.8-fold versus pristine FTS-MoS_2, achieving a 100.8% response at 400 ppb NO_2, together with a 17.2 ppb detection limit, high selectivity, and robust long-term and humidity-tolerant stability. Ex situ Raman spectroscopy supports an exposure-induced perturbation of the MoS_2 surface, whereas DFT calculations specifically predict stronger NO_2 adsorption and enhanced charge transfer in the presence of Pt single atoms. Collectively, these results establish ultrafast FTS as a powerful platform for active-site engineering in TMDs, offering a general and industrially viable strategy to construct single atom-decorated, defect-rich 2D catalysts for high-performance chemiresistive gas sensors and, more broadly, for catalytic and energy-conversion applications.

4 | Methods

4.1 | Materials

Ammonium tetrathiomolybdate ($(NH_4)_2MoS_4$, ATTM), $HAuCl_4{\bullet}3H_2O$, $IrCl_3$, $H_2PtCl_6{\bullet}6H_2O$, were purchased from Sigma-Aldrich. Chemicals were used without purification.

4.2 | Sample Preparation

To synthesize MoS_2 using the FTS process, we prepared an ATTM solution dispersed in deionized water. Specifically, 100 mg of ATTM was added to 1 mL of deionized water, followed by stirring for 1 h and sonicated for 30 min to disperse uniformly. A 100 µL of ATTM solution was then dropped onto a glass substrate (microslide glass, 76 × 52 × 1.2 mm) using a micropipette and subsequently dried on a hot plate at 80 °C for 2 h. The preparation procedure for noble metal-loaded MoS_2 followed the same steps as for MoS_2, with the exception of adding noble metal precursors (appropriate amount of $HAuCl_4{\bullet}3H_2O$, $IrCl_3$, and $H_2PtCl_6{\bullet}6H_2O$) to the ATTM solutions. The coating and drying processes were consistent with the ATTM solution. To synthesize MoS_2 via solvothermal method, 70 mg of ATTM was added to 40 mL of *N*,*N*-dimethylformamide (DMF) and stirred to achieve a uniform mixture. The resulting solution was transferred to a 50 mL Teflon-lined stainless-steel autoclave and heated at 200°C for 12 h with a ramping rate of 10 °C/min. After the solvothermal reaction, the black precipitates were collected by centrifugation at 4000 rpm and washed several times with DMF and ethanol to remove residual precursors.

4.3 | IPL System

The intense pulsed light (IPL) system comprises six key components: a simmer board, xenon lamp, capacitors, a DC power supply, an insulated-gate bipolar transistor (IGBT), and an infrared (IR) sensor system (Figure S60). The xenon lamp emits intense pulsed light with a broad wavelength spectrum ranging from 300 to 1000 nm (Figure S2). To initiate light emission, the simmer board ignites the xenon lamp, triggering a streamer breakdown. Following this, the capacitors (charged by the DC power supply to a target voltage (0–500 V)) are discharged through the IGBT, generating an arc breakdown that produces a high-intensity light pulse. The light power density can be precisely controlled by adjusting parameters such as the applied voltage, pulse duration, number of pulses, and the distance between the xenon lamp and the sample. The energy of the emitted pulses was quantified using a laser power meter (NOVA II, Ophir). During the process, the glass substrates were positioned 2–4 cm from the xenon lamp and irradiated for 10 ms at high energy densities of 10, 15, and 20 J cm^{-2} (1000, 1500, and 2000 W cm^{-2})

4.4 | Photothermal Temperature of ATTM

The IR sensor systems are introduced to detect the target temperature during the IPL process. The elaborate low temperature detected IR sensor (CTlaser 3MH2, Optris) detects from 200°C to 1500°C. The sensor produces a focused dot to measure the sample

temperature, with samples positioned at the proper distance. The measured analog signals are converted to digital signals by a data acquisition board (NI USB-6341 X series Multifunction DAQ, National Instruments). Since the temperature data were obtained with the emissivity value of the IR sensor at 1.00, these data were revised using tabulated values for the emissivity. The following equation (Equation 2) was used for all samples to calculate the revised temperature data.

$$\frac{1}{T_{\text{measured}}} = \frac{1}{T_{\text{corrected}}} + \frac{\lambda \ln\left(\frac{\varepsilon_{\text{measured}}}{\varepsilon_{\text{corrected}}}\right)}{C_2} \quad (2)$$

In this equation, T_{measured} represents the raw temperature data obtained from the sample, where the emissivity $\varepsilon_{\text{measured}}$ is set to 1.00 by the infrared (IR) sensor. $T_{\text{corrected}}$ is the temperature corrected for the actual emissivity. The term λ denotes the detection wavelength of the IR sensor, which is 2.3 μm for the CTlaser. Lastly, C_2 is the second radiant constant, with a value of 14387.8 μm K^{-1}. Since the temperature data were obtained with the emissivity set to 1.00, the data were revised using tabulated emissivity values for ammonium tetrathiomolybdate (ATTM). Based on IR camera detection at 2.3 μm, we examined absorbance at 2.3 μm in the FT-IR analysis of the ATTM. For the optically opaque ATTM coating ($T \approx 0$), the spectral emissivity at 2.3 μm was approximated using Kirchhoff's law as $\varepsilon \approx \alpha = 1 - R$, where R is the spectral reflectance at 2.3 μm.

4.5 | Material Characterization

Transmission electron microscopy (TEM), scanning transmission electron microscopy (STEM), and elemental analysis (energy-dispersive x-ray spectroscopy (EDS)) were conducted by transmission electron microscopy (Thermo Fisher, Talos F200X G2). EDS mapping data were processed with Velox software (Thermo Fisher). The crystal structures were carried out using a powder x-ray diffractometer (XRD) (Rigaku, D/MAX-RC 12 kW) using Cu Kα (λ = 1.54 Å) radiation. The chemical elements and bonding states were analyzed using x-ray photoelectron spectroscopy (XPS) (Sigma Probe, Thermo VG Scientific) with Al Ka radiation (1486.7 eV). Raman spectra was collected by a Horiba Jobin Yvon ARAMIS with a 514 nm excitation source. For the atomic-resolution imaging of a single atom on MoS_2, high-angle annular dark field scanning transmission electron microscopy (HAADF-STEM) was conducted with double-Cs-corrected transmission electron microscope (Spectra Ultra, Thermo Fisher). The microscope operated at an accelerating voltage of 200 kV and a beam convergence angle of 21.4 mrad. HAADF-STEM images were obtained with a screen current of ~ 20 pA, a resolution of 4096 × 4096 pixels, a pixel size of 6.249 pm, and a dwell time of 500 ns. For HAADF-STEM imaging, the detector's inner and outer collection angles were set to 52 and 200 mrad, respectively.

4.6 | Gas Sensing Measurements

The sensing materials, MoS_2 samples, were initially coated on the Al_2O_3 substrate using the drop-coating method. Each sensing material was dispersed in ethanol (2 mg in 100 μL) and drop-coated onto the substrate using a micropipette (2.5 μL) several times at room temperature. Gas sensing tests were conducted in a homemade gas sensing system featuring a 16-channel multiplexer (34902A, Agilent), a data acquisition system (34972A, Agilent) that measured resistance across 16 channels at 4-s intervals, and a mass flow control system for regulating gas concentration (Figure S61). Sensing tests were conducted in a humid environment (0%, 50%, and 75% RH), controlled by a mixture of water bubbler and balancing gas with mass flow controllers. Sensitivity, selectivity, and durability tests involved cyclic on/off exposures (30 and 60 min) to various gases and air, with response calculated as the change in resistance ($\Delta R/R_{\text{air}}$ [%]), indicating the ratio of baseline resistance in the air (R_{air}) to resistance change after gas exposure. The baseline resistances were stabilized over 3 h at room temperature. The sensor substrates consist of three main components: an alumina board, gold electrodes, and a platinum heater. The alumina substrate measures 2.5 mm × 2.5 mm with a thickness of 0.2 mm and printed interdigitated Au electrodes (width: 25 μm, spacing: 70 μm). The ex situ Raman spectrometer was performed with the sensing materials after exposure for 1 h to 5 ppm of NO_2.

4.7 | Computational Details

The spin-polarized DFT calculations were conducted using Vienna Ab-initio Simulation Package (VASP) with the projector-augmented wave (PAW) method [49–51]. Wave functions were represented using a plane-wave basis set with an energy cutoff of 520 eV. Perdew–Bruke–Ernzerhof (PBE) functional was used to calculate the exchange-correlation energy [52]. DFT-D3 method with zero-damping function was employed to describe van der Waals interactions [53]. The convergence criterions for electronic and ionic step were set to 10^{-6} eV, and −0.02 eV/Å, respectively. The number of valence electrons was set to 5, 6, 6, 6, 9, 10, and 11 for N, O, Mo, S, Ir, Pt, and Au, respectively.

The FTS-MoS_2 slab model for adsorption energies and Bader charge differences was constructed with an interface between MoS_2 and Mo_2S_3 and a sulfur vacancy (V_S). MoS_2/Mo_2S_3 interface was generated by placing the MoS_2 (001) slab on the Mo_2S_3 (-101) slab with interface builder in QuantumATK [54] (Figure S19). To accommodate lattice mismatch, a mean absolute strain of 2.44% was introduced with directional strains $\varepsilon_{11} = -2.41\%$, $\varepsilon_{22} = 0.89\%$ and $\varepsilon_{12} = -4.02\%$. A vacuum region of 15Å was introduced along the z-axis. 1 ×5 ×1 Γ-centered k-point grid was used to sample the Brillouin zone for these slab structures.

Adsorption energies of adsorbate (single atoms and NO_2) (E_{ads}) was calculated using the Equation 3:

$$E_{\text{ads}} = E_{\text{slab}^*} - (E_{\text{slab}} + E_{\text{adsorbate}}) \quad (3)$$

where E_{slab^*}, E_{slab}, and $E_{\text{adsorbate}}$ are total energies of slab model with adsorbate, bare slab and the isolated adsorbate, respectively. The energies of the isolated absorbate were calculated in a 10 × 10 × 10 $Å^3$ cubic cell with a 1 × 1 × 1 Γ-centered k-point grid. VESTA software was utilized to illustrate crystal structures and charge density difference ($\Delta\rho$) maps for NO_2 adsorption were computed using the Equation 4:

$$\Delta\rho = \rho_{\text{slab}^*} - \left(\rho_{\text{slab}} + \rho_{NO_2}\right) \quad (4)$$

where ρ_{slab*}, ρ_{slab}, and ρ_{NO_2} are charge density of NO_2 adsorbed slab, bare MoS_2 or M_{SA}-MoS_2 slab and NO_2 molecule. Isosurface level of charge density difference map was set to 0.01 e/Å^3.

Author Contributions

I.-D.K. and D.-H.K. supervised the overall project. E.S. conceived the work, designed the whole project, including conceptualization and experiments, and wrote the manuscript. J.C. and J.M.Y. carried out S/TEM measurements. W.C., S.P., and C.-W.L carried out DFT calculations. S.W. helped to carry out gas sensing measurements. M.S., M.S.K, C.P., and J.W.B assisted the measurements and material synthesis. S.-Y.C. assisted the IPL process. All authors discussed the results and assisted during manuscript preparation.

Acknowledgements

This work was supported by the National Research Foundation of Korea (NRF) grant funded by the Korea government (MSIT) (RS-2024-00357296, RS-2024-00435493, RS-2023-00236572, and RS-2022-NR070288).

Conflicts of Interest

The authors declare no conflicts of interest.

Data Availability Statement

The data that support the findings of this study are available on request from the corresponding author. The data are not publicly available due to privacy or ethical restrictions.

References

1. S. Manzeli, D. Ovchinnikov, D. Pasquier, O. V. Yazyev, and A. Kis, "2D transition Metal Dichalcogenides," *Nature Reviews Materials* 2 (2017): 17033.

2. G. Mirabelli, C. McGeough, M. Schmidt, et al., "Air Sensitivity of MoS2, MoSe2, MoTe2, HfS2, and HfSe2," *Journal of Applied Physics* 120 (2016): 125102.

3. B. Cho, M. G. Hahm, M. Choi, et al., "Charge-transfer-based Gas Sensing Using Atomic-layer MoS2," *Scientific Reports* 5 (2015): 8052.

4. S.-Y. Cho, S. J. Kim, Y. Lee, et al., "Highly Enhanced Gas Adsorption Properties in Vertically Aligned MoS2 Layers," *ACS Nano* 9 (2015): 9314–9321.

5. J. Kibsgaard, Z. Chen, B. N. Reinecke, and T. F. Jaramillo, "Engineering the Surface Structure of MoS2 to Preferentially Expose Active Edge Sites for Electrocatalysis," *Nature Materials* 11 (2012): 963–969.

6. J. Sun, X. Li, W. Guo, et al., "Synthesis Methods of Two-Dimensional MoS2: A Brief Review," *Crystals* 7 (2017): 198.

7. L. Fei, S. Lei, W.-B. Zhang, et al., "Direct TEM Observations of Growth Mechanisms of Two-dimensional MoS2 Flakes," *Nature Communications* 7 (2016): 12206.

8. L. Liu, T. Chen, and Z. Chen, "Understanding the Dynamic Aggregation in Single-Atom Catalysis," *Advanced Science* 11 (2024): 2308046.

9. X. Wang, Y. Zhang, J. Wu, et al., "Single-Atom Engineering to Ignite 2D Transition Metal Dichalcogenide Based Catalysis: Fundamentals, Progress, and beyond," *Chemical Reviews* 122 (2021): 1273–1348.

10. P. Zhao, X. Wu, Y. Zhang, et al., "Ultrafast Thermal Engineering in Energy Materials: Design, Recycling, and Future Directions," *ACS Nano* 19 (2025): 17199–17227.

11. L. Yan, C. Wang, and X. Yin, "A Review of Methods for Improving Microwave Heating Uniformity," *Microwave* 1 (2025): 12.

12. K. C. Phillips, H. H. Gandhi, E. Mazur, and S. Sundaram, "Ultrafast Laser Processing of Materials: A Review," *Advances in Optics and Photonics* 7 (2015): 684.

13. H. S. Lim, S. J. Kim, H. W. Jang, and J. A. Lim, "Intense Pulsed Light for Split-second Structural Development of Nanomaterials," *Journal of Materials Chemistry C* 5 (2017): 7142–7160.

14. A. Abdelhafiz, A. Tanvir, M. Zeng, et al., "Pulsed Light Synthesis of High Entropy Nanocatalysts With Enhanced Catalytic Activity and Prolonged Stability for Oxygen Evolution Reaction," *Advanced Science* 10 (2023): 2300426.

15. D.-H. Kim, J.-H. Cha, S. Chong, et al., "Flash-Thermal Shock Synthesis of Single Atoms in Ambient Air," *ACS Nano* 17 (2023): 23347–23358.

16. J. Baek, Y. Jiang, D. Ka, et al., "Ultrafast Photoflash Synthesis of High-Entropy Oxide Nanoparticles," *ACS Nano* 19 (2025): 5839–5850.

17. D. Jeon, H. Shin, J.-H. Cha, et al., "Photothermal Annealing-Enabled Millisecond Synthesis of Carbon Nanoonions and Simultaneous Single-Atom Functionalization," *ACS Nano* 19 (2025): 34235–34247.

18. J. H. Cha, S. H. Cho, D. H. Kim, et al., "Flash-Thermal Shock Synthesis of High-Entropy Alloys Toward High-Performance Water Splitting," *Advanced Materials* 35 (2023): 2305222.

19. E. Shin, D.-H. Kim, J.-H. Cha, et al., "Ultrafast Ambient-Air Exsolution on Metal Oxide via Momentary Photothermal Effect," *ACS Nano* 16 (2022): 18133–18142.

20. A. Gupta, K. Ankireddy, B. Kumar, et al., "Intense Pulsed Light, a Promising Technique to Develop Molybdenum Sulfide Catalysts for Hydrogen Evolution," *Nanotechnology* 30 (2019): 175401.

21. M. Xu, J. Gao, J. Song, et al., "Programmable Patterned MoS2 Film by Direct Laser Writing for Health-related Signals Monitoring," *Iscience* 24 (2021): 11.

22. R. I. Walton, A. J. Dent, and S. J. Hibble, "In Situ Investigation of the Thermal Decomposition of Ammonium Tetrathiomolybdate Using Combined Time-Resolved X-ray Absorption Spectroscopy and X-ray Diffraction," *Chemistry of Materials* 10 (1998): 3737–3745.

23. L. Fei, M. Xu, J. Jiang, et al., "Three-dimensional Macroporous Graphene Monoliths With Entrapped MoS2 Nanoflakes From Single-step Synthesis for High-performance Sodium-ion Batteries," *RSC Advances* 8 (2018): 2477.

24. N. Alinejadian, S. H. Kazemi, and I. Odnevall, "SLM-processed MoS_2/Mo_2S_3 Nanocomposite for Energy Conversion/Storage Applications," *Scientific Reports* 12 (2022): 5030.

25. S. Mattila, J. A. Leiro, M. Heinonen, and T. Laiho, "Core Level Spectroscopy of MoS2," *Surface Science* 600 (2006): 5168–5175.

26. S. E. More, S. A. Raut, S. Premkumar, et al., "Oxidation Behavior of Iron and Binder-mixed Iron: Insights from TGA–DSC and In Situ XRD Analysis for Field Emission Application," *Materials Advances* 7 (2026): 198.

27. E. Shin, D. H. Kim, M. Sagong, et al., "Flash Thermal Shock Synthesis of Heterostructured Transition Metal Dichalcogenides and Carbides in Milliseconds," *Advanced Materials* 37, no. 30 (2025): 2419790.

28. S. Sarkar, I. Maity, H. Pradeepa, et al., "Anharmonicity in Raman-active Phonon Modes in Atomically Thin MoS2," *Physical Review B* 101 (2020): 205302.

29. P. Cao, J. Peng, S. Liu, et al., "Tuning the Composition and Structure of Amorphous Molybdenum Sulfide/Carbon Black Nanocomposites by Radiation Technique for Highly Efficient Hydrogen Evolution," *Scientific Reports* 7 (2017): 16048.

30. W. Wang, C. Yang, L. Bai, M. Li, and W. Li, "First-Principles Study on the Structural and Electronic Properties of Monolayer MoS2 With S-Vacancy under Uniaxial Tensile Strain," *Nanomaterials* 8 (2018): 74.

31. A. M. Z. Tan, C. Freysoldt, and R. G. Hennig, "Stability of Charged Sulfur Vacancies in 2D and Bulk MoS2 from Plane-wave Density Func-

tional Theory With Electrostatic Corrections," *Physical Review Materials* 4 (2020): 064004.

32. S. Park, A. Lee, K.-H. Choi, et al., "Layer-Selective Synthesis of MoS 2 and WS 2 Structures Under Ambient Conditions for Customized Electronics," *ACS Nano* 14 (2020): 8485–8494.

33. N. Aguilar, M. Atilhan, and S. Aparicio, "Single Atom Transition Metals on MoS2 Monolayer and Their Use as Catalysts for CO2 Activation," *Applied Surface Science* 534 (2020): 147611.

34. H. Liu, D. Grasseschi, A. Dodda, et al., "Spontaneous Chemical Functionalization via Coordination of Au Single Atoms on Monolayer MoS_2," *Science Advances* 6, no. 49 (2020): abc9308.

35. Z. Shi, X. Zhang, X. Lin, et al., "Phase-dependent Growth of Pt on MoS2 for Highly Efficient H2 Evolution," *Nature* 621 (2023): 300–305.

36. J. Ji, J. Wang, J. S. Reinhold, et al., "Single-atom Iridium Doped Ultrathin MoS2 Layers as a Highly Efficient Catalyst for the Hydrodeoxygenation of 5-hydroxymethylfurfural," *Chemical Engineering Science* 291 (2024): 119896.

37. C. Chen, C. Ye, X. Zhao, et al., "Supported Au Single Atoms and Nanoparticles on MoS2 for Highly Selective CO2-to-CH3COOH Photoreduction," *Nature Communications* 15 (2024): 7825.

38. R. K. Tiwari, J. Yang, M. Saeys, and C. Joachim, "Surface Reconstruction of MoS2 to Mo2S3," *Surface Science* 602 (2008): 2628–2633.

39. Z. Wang, G. Lu, T. Wei, et al., "Synergy of Single Atoms and Sulfur Vacancies for Advanced Polysulfide–iodide Redox Flow Battery," *Nature Communications* 16 (2025): 2885.

40. X. Du, B. Zhang, Y. Lian, X. Jiang, Y. Li, and D. Jiang, "A Bulit-in Self-calibration Ratiometric Self-powered Photoelectrochemical Sensor for High-precision and Sensitive Detection of Microcystin-RR," *Microchimica Acta* 191, no. 7 (2024): 379.

41. J. Xu, G. Shao, X. Tang, et al., "Frenkel-defected Monolayer MoS2 Catalysts for Efficient Hydrogen Evolution," *Nature Communications* 13 (2022): 2193.

42. Y. Zhou, J. Zhang, E. Song, et al., "Enhanced Performance of in-plane Transition Metal Dichalcogenides Monolayers by Configuring Local Atomic Structures," *Nature Communications* 11 (2020): 2253.

43. K. Jiang, M. Luo, Z. Liu, et al., "Rational Strain Engineering of Single-atom Ruthenium on Nanoporous MoS2 for Highly Efficient Hydrogen Evolution," *Nature Communications* 12, no. 1 (2021): 1687.

44. Y. Xia, C. Hu, S. Guo, et al., "Sulfur-Vacancy-Enriched MoS 2 Nanosheets Based Heterostructures for Near-Infrared Optoelectronic NO 2 Sensing," *ACS Applied Nano Materials* 3, no. 1 (2019): 665–673.

45. J. Yan, Y. Wang, C. Yang, H. Deng, and N. Hu, "MoS2/MoO3 heterojunctions Enabled by Surface Oxidization of MoS2 Nanosheets for High-performance Room-temperature NO2 Gas Sensing," *Journal of Alloys and Compounds* 976 (2024): 173208.

46. J. W. Baek, E. Shin, J. Lee, D.-H. Kim, S.-J. Choi, and I.-D. Kim, "Present and Future of Emerging Catalysts in Gas Sensors for Breath Analysis," *ACS sensors* 10 (2024): 33.

47. J. H. Cha, D. H. Kim, C. Park, et al., "Low-Thermal-Budget Doping of 2D Materials in Ambient Air Exemplified by Synthesis of Boron-Doped Reduced Graphene Oxide," *Advanced Science* 7, no. 7 (2020): 1903318.

48. G. Henkelman, A. Arnaldsson, and H. Jónsson, "A Fast and Robust Algorithm for Bader Decomposition of Charge Density," *Computational Materials Science* 36 (2006): 354–360.

49. G. Kresse and J. Furthmüller, "Efficient Iterative Schemes for Ab Initio Total-energy Calculations Using a Plane-wave Basis Set," *Physical Review B* 54 (1996): 11169–11186.

50. P. E. Blöchl, "Projector Augmented-wave Method," *Physical Review B* 50 (1994): 17953.

51. G. Kresse and D. Joubert, "From Ultrasoft Pseudopotentials to the Projector Augmented-wave Method," *Physical Review B* 59 (1999): 1758–1775.

52. J. P. Perdew, K. Burke, and M. Ernzerhof, "Generalized Gradient Approximation Made Simple," *Physical Review Letters* 77 (1996): 3865–3868.

53. S. Grimme, J. Antony, S. Ehrlich, and H. Krieg, "A Consistent and Accurate Ab Initio Parametrization of Density Functional Dispersion Correction (DFT-D) for the 94 Elements H-Pu," *Journal of Chemical Physics* 132 (2010): 154104.

54. S. Smidstrup, T. Markussen, P. Vancraeyveld, et al., "QuantumATK: an Integrated Platform of Electronic and Atomic-scale Modelling Tools," *Journal of Physics-Condensed Matter* 32 (2020): 015901.

Supporting Information

Additional supporting information can be found online in the Supporting Information section.

Supporting File: adma75106-sup-0001-SuppMat.docx.